DTU Library

Contrast-enhanced ultrasound imaging using capacitive micromachined ultrasonic transducers

Øygard, Sigrid Husebø; Ommen, Martin Lind; Tomov, Borislav Gueorguiev; Diederichsen, Søren Elmin; Thomsen, Erik Vilain; Stuart, Matthias Bo; Larsen, Niels Bent; Jensen, Jørgen Arendt

Link back to DTU Orbit

Contrast-enhanced ultrasound imaging using capacitive micromachined ultrasonic transducers

Sigrid H. Øygard,[a] Martin L. Ommen, Borislav G. Tomov, Søren E. Diederichsen, Erik V. Thomsen, Matthias B. Stuart, Niels B. Larsen, and Jørgen A. Jensen

Department of Health Technology, Technical University of Denmark, DK-2800 Lyngby, Denmark

Capacitive micromachined ultrasonic transducers (CMUTs) have a nonlinear relationship between the applied voltage and the emitted signal, which is detrimental to conventional contrast enhanced ultrasound (CEUS) techniques. Instead, a three-pulse amplitude modulation (AM) sequence has been proposed, which is not adversely affected by the emitted harmonics. In this paper, this is shown theoretically, and the performance of the sequence is verified using a 4.8 MHz linear CMUT array, and a comparable lead zirconate titanate (PZT) array, across 6 V to 60 V applied AC voltage. CEUS images of the contrast agent SonoVue flowing through a 3D printed hydrogel phantom showed an average enhancement in contrast-to-tissue ratio (CTR) between B-mode and CEUS images of 49.9 dB and 37.4 dB for the PZT array and CMUT, respectively. Furthermore, hydrophone recordings of the emitted signals showed that the nonlinear emissions from the CMUT did not significantly degrade the cancellation in the compounded AM signal, leaving an average of 2 % of the emitted power between 26 V and 60 V AC. Thus, it is demonstrated that CMUTs are capable of CEUS imaging independent of the applied excitation voltage when using a three-pulse AM sequence.

[XYZ]

I. INTRODUCTION

Recently, capacitive micromachined ultrasonic transducers (CMUTs) have become available as an alternative to the more conventional piezoelectric transducers (Haller and Khuri-Yakub, 1994; Oralkan *et al.*, 2002). CMUTs offer sensitivity features that are particularly suitable for microbubble contrast-enhancement imaging, with low transmit pressure, yet high receive sensitivity (Oralkan *et al.*, 2002). Contrast enhanced ultrasound (CEUS) imaging with microbubble contrast agents is used clinically to study the blood's wash-in and wash-out time in organs (Dietrich *et al.*, 2018), to quantify the blood-flow velocity using time-intensity curves (Tang *et al.*, 2011), and, most recently, to image blood-flow through capillaries beyond the diffraction limit, through super-resolution ultrasound imaging (SRI) (Christensen-Jeffries *et al.*, 2015; Errico *et al.*, 2015). CEUS imaging with a CMUT is a combination of two nonlinear processes; the spectral content of the emission from a CMUT is nonlinearly related to its excitation voltage (Novell *et al.*, 2008), and the spectral content of the scattering of the excitation by the microbubble contrast agents is nonlinearly related to the acoustic pressure (Leighton, 1994). This combination poses some challenges to the conventional CEUS techniques, and the viability of CEUS imaging using CMUTs has been questioned (Martin *et al.*, 2014).

CMUTs emit ultrasound by applying an AC voltage potential across thin plates suspended on top of nanometer to micrometer sized cavities. The technology offers great design flexibility (Kamaya *et al.*, 2013), making it possible to produce transducers with several advantageous features for CEUS imaging. Firstly, the transducer can achieve wide bandwidth, resulting in high axial resolution (Kamaya *et al.*, 2013). For SRI, where separation of the microbubbles within each image frame is essential, this could enable SRI with a higher number of resolved microbubbles within each frame, and thus a lower acquisition time. The wide bandwidth would also facilitate detection of higher harmonics scattered by the microbubbles, often utilized in the pulse inversion (PI) technique. Secondly, CMUTs can produce a low emitted pressure, suitable for exciting microbubbles without destroying them (Eckersley *et al.*, 2005), whilst maintaining a high receive sensitivity (Savoia *et al.*, 2012). However, the drawback of CMUT technology is that the electrostatic force driving the excitation causes the emitted signal to contain considerable harmonic components (Lohfink and Eccardt, 2005a). The amount of harmonic content produced by the transducer is dependent on the ratio of the applied AC voltage to the applied DC voltage (Novell *et al.*, 2008), which renders the transducer incapable of removing of tissue-generated signals using conventional CEUS techniques.

CEUS imaging achieves high contrast by removing the signal scattered by the tissue from that scattered by the microbubbles. The most common techniques used to remove the tissue signal are PI, amplitude modulation

---

[a]soygard@gmail.com

(AM), and singular value decomposition (SVD). The first two utilize the fact that when a bubble is insonified, it will scatter the sound nonlinearly (Miller, 1981). SVD is a spatiotemporal filtering technique, which utilizes the bubble's high scattered intensity and temporally transient behavior to separate the bubbles from the tissue (Errico *et al.*, 2015). These techniques are thus capable of removing the linearly scattered signals caused by the tissue surrounding the contrast agents. PI combines the responses from two excitations with opposite signs (Simpson *et al.*, 1999). Conventionally, AM is achieved by combining the response from two excitations, one with half the amplitude of the next (Brock-Fischer *et al.*, 1996). Both the difference in amplitude and difference in polarity will cause the CMUT to emit harmonics that differ between the emissions, which conventional AM and PI will not be able to remove. Using such sequences with CMUTs will therefore result in poor contrast in the CEUS images (Fouan and Bouakaz, 2016; Oygard *et al.*, 2020a). Several attempts have been made to overcome this issue by altering the frequency content of the emitted pulse (Lei *et al.*, 2016; Zhou *et al.*, 2003), but such approaches are not necessarily compatible with the bipolar pulsers often found in commercial scanners. Moreover, these methods rely on all elements in the probe behaving identically, which is often not the case. However, Fouan and Bouakaz (Fouan and Bouakaz, 2016) have proposed that CEUS imaging can be obtained using simple sinusoidal excitations by implementing a three-pulse AM sequence. In this sequence, the difference in amplitude between emissions, which is needed to preserve the nonlinear back-scattering from the microbubbles, is achieved by emitting once with the full active aperture, once with the odd-numbered elements, and once with the even-numbered elements. Fouan and Bouakaz (Fouan and Bouakaz, 2016) shows that for a single transmit voltage of 20 V applied to a CMUT, a 15 dB improvement in contrast-to-tissue ratio (CTR) was achieved, compared with an AM sequence with scaled voltage. A similar approach has been studied in (Oygard *et al.*, 2020a), where it was shown that a two-pulse AM sequence with halving of the active elements resulted in better contrast than conventional PI imaging. The contrast of CEUS images is influenced by the power of the AM signal compared with the power of any remaining signal scattered by tissue, often quantified by CTR (Bouakaz *et al.*, 2002). Since the applied voltage and polarity to each emitting element is constant for all emissions in these modified AM sequences, the theory predicts that the emitted signals therefore contain the same harmonics. This indicates that the increasing harmonic content resulting from increased applied AC voltage does not affect the performance of the imaging technique.

This paper investigates the two-pulse and three-pulse AM sequence at a wide range of transmit voltages, corresponding to varying nonlinear components in the emissions. It is hypothesized that the amount of nonlinear harmonics in the emitted signal does not affect the efficiency of these modified AM techniques. This is demonstrated theoretically, and verified with measurements. The method's ability to cancel linear components is measured using hydrophone recordings, and its contrast enhancement is assessed using CEUS imaging of a microflow phantom with SonoVue contrast agents. The measurements are made using a linear CMUT array produced in house, and, for reference, using a corresponding commercial lead zirconate titanate (PZT) array.

II. THEORY

A. Emission from a CMUT

The propagation of sound waves from a CMUT array is induced by applying an AC voltage, V_{AC}, across the CMUT cells. This causes a time-varying deflection, driven by electrostatic force on the cell plates. (Certon *et al.*, 2005). The acoustic pressure radiated from a circular cell plate is proportional to the resulting displacement of the plate (Kinsler *et al.*, 1982), and the relationship between the applied voltage and the displacement is governed by a nonlinear differential equation (Lohfink and Eccardt, 2005b). Analytic evaluation of this equation is not straight forward, but several authors have studied the relationship numerically (Certon *et al.*, 2005; Lohfink and Eccardt, 2005b; Meynier *et al.*, 2010). It has been shown that the emitted sound pressure from CMUTs contain harmonics to the applied excitation frequency (Lohfink and Eccardt, 2005b; Novell *et al.*, 2009). Thus, when the applied V_{AC} is a simple sinusoid at some excitation frequency, ω_0, the resulting emitted pressure, $p(t)$, can be expressed as

$$
p(t) = \alpha_0 \sin(\omega_0 t)
$$
$$
+ \sum_{h=2}^{\infty} \alpha_h \sin(h\omega_0 t + \phi_h), \quad \begin{cases} h \in \mathbb{Z}, \\ \alpha_h \in \mathbb{R}, \end{cases} \quad (1)
$$
$$
= p_L(t) + \sum_{h=2}^{\infty} p_H(t) \quad (2)
$$

Here, t is time, α is some amplitude, h is a harmonic index, ϕ is a phase difference. Since α_h can be any real number, including zero, this notation is applicable even when only certain harmonics are present in the emitted signal. A compact form of (1) is given in (2), where $p_L(t)$ is the linear part, i.e. the component of the signal which has the same frequency content as the applied ω_0, and $\sum p_H(t)$ is the harmonics. The amplitude and phase of the harmonics are determined by the complex dynamics of the CMUT array, and are not further described here. Notably, it has been shown that the amount of harmonic content in the emitted pressure wave depends on the ratio of the amplitude of the applied V_{AC} to the applied DC voltage (Novell *et al.*, 2009), and CMUTs are therefore said to be inherently nonlinear. However, it will here be shown that the nature of the harmonics does not affect the effectiveness of the three-pulse AM sequence.

In the three-pulse AM sequence proposed by Fouan and Bouakaz (Fouan and Bouakaz, 2016), a pulse of full amplitude, p_A, is emitted, followed by two pulses

of halved amplitude, p_B and p_C. The applied voltage is constant across all three emissions, and the two half amplitudes are made by halving the number of active elements compared with the full emission, spread across the same active aperture width. Thus, the three emitted pulses are

$$p_A(t) = \alpha_0 \sin(\omega_0 t) + \sum_{h=2}^{\infty} \alpha_h \sin(h\omega_0 t + \phi_h), \quad (3)$$

$$p_B(t) = 0.5\left[\alpha_0 \sin(\omega_0 t) + \sum_{h=2}^{\infty} \alpha_h \sin(h\omega_0 t + \phi_h)\right], \quad (4)$$

$$p_C(t) = 0.5\left[\alpha_0 \sin(\omega_0 t) + \sum_{h=2}^{\infty} \alpha_h \sin(h\omega_0 t + \phi_h)\right]. \quad (5)$$

B. The amplitude modulation technique

When the microbubbles are insonified with an ultrasound pulse, the reflections contain harmonics of the incident frequency. Eckersley et al. (Eckersley *et al.*, 2005) show that the nonlinear reflections can be modeled as a polynomial expansion of the incident wave, as

$$y(t) = a_1 p_i(t) + a_2 p_i^2(t) + a_3 p_i^3(t) + \dots + a_{\infty} p_i^{\infty}(t). \quad (6)$$

Here, $y(t)$ is the reflected signal, $p_i(t)$ is the incident pressure wave on the bubble, and a_i are reflection coefficients determining the different nonlinear contributions, where a_1 represents the linear reflection and $a_{i>1}$ represents the nonlinear reflections. To suppress the linear component of the emitted signal, while preserving the nonlinear components at the fundamental, the reflected signals are combined as

$$y_{AM}(t) = y_A(t) - y_B(t) - y_C(t), \quad (7)$$

where y_{AM} is the remaining three-pulse amplitude modulation signal, and y_A, y_B, y_C are the scattered signals caused by the three emissions. If instead, only 2 emissions are used the combination is made as

$$y_{AM}(t) = y_A(t) - 2 \cdot y_B(t). \quad (8)$$

C. Amplitude modulation with a CMUT

By assuming that no distortion of the signal occurs between the emission and the bubble position, we can apply (6) to the tree emissions given in (3) - (5) before applying (7). By expressing the pressure waves in their compact form and limiting the polynomial expansion to third order for simplicity, this gives

$$y_{AM}(t) = a_1 p_A + a_2 p_A{}^2 + a_3 p_A{}^3 - a_1 p_B - a_2 p_B{}^2 - a_3 p_B{}^3 - a_1 p_C - a_2 p_C{}^2 - a_3 p_C{}^3. \quad (9)$$

Then, by expanding to the long form of (3) - (5), setting $\alpha_0 = 1$, working through the algebra (shown in more detail in the appendix) gives

$$\begin{aligned}
y_{AM}(t) =&\, 0.5\, a_2 \sin(\omega_0 t)^2 \\
&+ 0.5\, a_2 \left(\sum_{h=2}^{\infty} \alpha_h \sin(h\omega_0 t + \phi_h)\right)^2 \\
&+ a_2 \sin(\omega_0 t)\left(\sum_{h=2}^{\infty} \alpha_h \sin(h\omega_0 t + \phi_h)\right) \\
&+ 2.25\, a_3 \sin(\omega_0 t)\left(\sum_{h=2}^{\infty} \alpha_h \sin(h\omega_0 t + \phi_h)\right)^2 \\
&+ 2.25\, a_3 \sin(\omega_0 t)^2\left(\sum_{h=2}^{\infty} \alpha_h \sin(h\omega_0 t + \phi_h)\right) \\
&+ 0.75\, a_3 \left(\sum_{h=2}^{\infty} \alpha_h \sin(h\omega_0 t + \phi_h)\right)^3 \\
&- 0.1875\, a_3 \sin(3\omega_0 t) \\
&+ 1.5\, a_3 \sin(\omega_0 t). \quad (10)
\end{aligned}$$

Two important observations can be made about (10). Firstly, it reveals a subtle, but, essential property of AM imaging; the remaining signal lacks any linearly scattered components, yet, the last term of (10) contains energy at the fundamental frequency. The reflection coefficient a_3 indicates that this component is caused by the nonlinear scattering properties of the microbubbles. Secondly, it is observed that this cancellation of the linearly scattered signal was attained despite the nonlinear nature of the CMUT. Although harmonics to the fundamental frequency are emitted, as seen in (3) - (5), (10) does not contain any emitted harmonics with the linear reflection coefficient a_1. This shows that when the emitted signals are reflected only linearly, the AM compounding cancels all of these terms. Some emitted harmonics remain in the y_{AM} signal, but, these terms all carry the reflection coefficients a_2 or a_3, meaning that the signals have been nonlinearly scattered by the microbubble. Notably, the fact that these emitted harmonics remain in the y_{AM} signal has not impaired the efficiency of the AM theory. Moreover, although the amplitude and phase of the emitted harmonics will be affected by the amplitude of V_{AC}, this does not affect the cancellation of linearly scattered signals. Because of this, when using the AM modality to image *in vivo* with a CMUT, it is possible to filter out linear scattering from tissue whilst attaining reflections from the microbubbles at the emitted frequency. Thus, it is shown theoretically that CEUS imaging with a CMUT using the three-pulse AM sequence is achievable.

III. METHODS

To verify the outcome of the theoretical evaluation shown in Section II, the ability of a linear CMUT array to cancel received linear components while preserving nonlinearly scattered signal was assessed using three mea-

TABLE I. Specifications of the transducers.

|	CMUT	PZT
Total number of elements	192	192
Center frequency	$4.8\,\mathrm{MHz}$	$5.2\,\mathrm{MHz}$
Pitch (p)	$0.2\,\mathrm{mm}$	$0.2\,\mathrm{mm}$
Kerf	$0.02\,\mathrm{mm}$	$0.02\,\mathrm{mm}$
Maximum tolerable AC voltage	$60\,\mathrm{V}$	$100\,\mathrm{V}$
Applied DC voltage	$190\,\mathrm{V}$	N/A

FIG. 1. An illustration of the experimental set-up showing how the phantom and tissue-mimicking material are positioned under the transducer and held in place by a brace. The transducer sits directly above the phantom and tissue-mimicking material, in contact with the water.

surement set-ups. Firstly, an experimental set-up was designed to quantify CTR. Section III A outlines the design of the set-up. Contrast enhanced AM images were collected using a synthetic aperture imaging sequence on a CMUT and a PZT probe, further described in Section III B. Subsequently, the CTR was calculated for all the collected images, as detailed in Section III C. Secondly, Section III D describes how the emitted signal from the transducers were recorded using a hydrophone, and used to determine the peak-negative-pressure (PNP) and the power annihilation ratio. Lastly, Section III E describes how the signal-to-noise ratio of the two probes were evaluated to fairly compare the CMUT's and PZT arrays's performance.

A. CEUS imaging set-up

The experimental set-up used to quantify CTR consisted of a microflow phantom and a block of tissue-mimicking material. An illustration of the measurement set-up can be seen in Fig. 1. The microflow phantom was 3D printed in a PEGDA $700\,\mathrm{g\,mol^{-1}}$ hydrogel block using stereo-lithography. A hollow channel of $200\,\mu\mathrm{m}$ in diameter was printed inside the phantom, as shown in Fig. 2. The fabrication process of the phantom has been described in (Ommen *et al.*, 2018). The phantom was held in place by a brace next to a block of tissue-mimicking material made of polyvinyl alcohol cryogel (Lai *et al.*, 2013; Olesen *et al.*, 2018), resulting in scattering properties similar to that of human tissue. The ensemble was placed in a water bath, which was lined with an acoustic absorber. The phantom was positioned so that the center of the flow channel was $25\,\mathrm{mm}$ below the surface of the transducer. A low pressure flow pump (neMESYS 290N, Cetoni) fitted with a syringe of SonoVue microbubble contrast agents, diluted 1:10 with saline, was connected to the phantom and used to pump microbubbles through the phantom.

B. Image acquisition

The phantom and tissue-mimicking material was imaged using a linear CMUT (Diederichsen, 2020) and, as
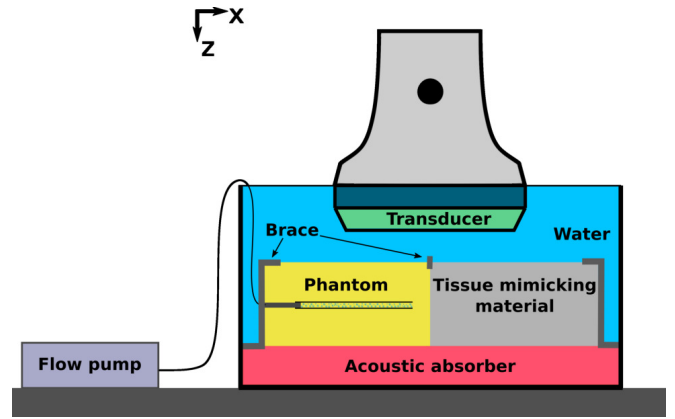
a reference, a commercial linear PZT array of equivalent design dimensions, using a Verasonics research scanner (Verasonics Vantage 256). The specifications of the probes are given in Table I. The set-up was imaged using a synthetic aperture sequence (Jensen *et al.*, 2006) with low intensity diverging wave propagation. A summary of the sequence parameters are given in Table II. The transducers emitted a 2 cycle sine wave at $4.8\,\mathrm{MHz}$, with 32 active elements in each full amplitude emission, and with a pulse repetition frequency of $1000\,\mathrm{Hz}$. The sequence consisted of emissions from $n = 13$ virtual sources placed $16\,\mathrm{mm}$ behind the transducer surface. The lateral
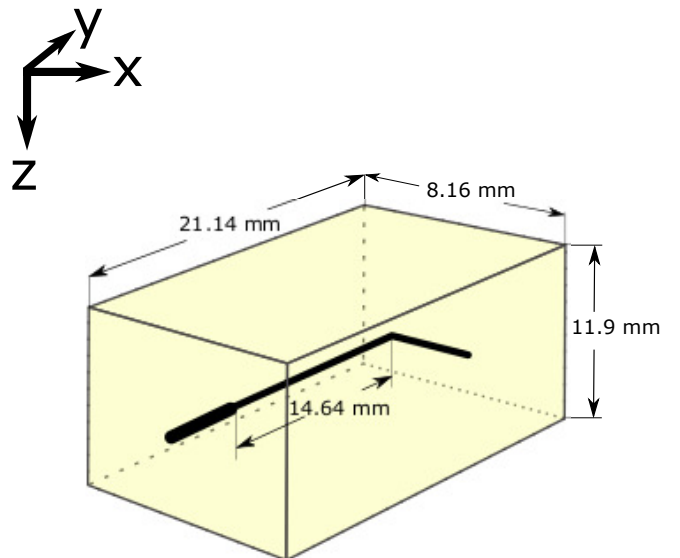

FIG. 2. An illustration of the phantom, where the bold black line illustrates the internal channel.

TABLE II. Parameters of the synthetic aperture sequence.

Pulse repetition frequency	1000 Hz
Number of active elements	32
Emission frequency	4.8 MHz
Focal distance	-16 mm
Receive F-number	1
Number of emissions (n)	13
Number of cycles in emission	2
Number of elements separating emissions (s)	13

positions of the virtual sources were given by

$$x_i = s \cdot i \cdot p, \forall i \in \mathbb{Z} : i \in [-\frac{(n-1)}{2}, \frac{(n-1)}{2}], \qquad (11)$$

where s denotes the number of elements separating the lateral positions of two virtual sources, i is emission index, p is the transducer pitch, and $x_i = 0$ lays in the middle of the transducer. The three emissions described in (3) - (5) are referred to as the minor sequence. The minor sequence was emitted once by each virtual source at each x_i to make a full image frame.

The sequence was used to quantify how the CTR in the resulting images vary with the applied AC voltage. The lowest V_{AC} was 6 V, at which the imaging system approaches its noise floor. For the CMUT, V_{AC} was then increased in steps of 10 V until the maximum tolerable AC voltage of the probe, as given in Table I, was reached. Additionally, a constant DC voltage of 190 V was applied to the CMUT, as specified in (Diederichsen, 2020). For the PZT array, the same voltage range was used, from 6 V to the probe's maximum tolerable voltage. But, the step size was reduced to 3 V between 6 V and 15 V. This was done to ensure a good population of data-points within the overlapping range of PNP for the two probes, since the relationship between applied voltage and PNP is not linear.

The SonoVue solution was allowed to flow continuously through the phantom channel at $0.6 \, \mu L \, s^{-1}$, while 10 image frames were collected at each V_{AC}. To avoid degradation of the microbubbles during the collection of the 10 frames, a pause of 15 s was inserted between each frame to allow a fresh batch of microbubbles to flow into the phantom. A fresh syringe of diluted contrast agents were prepared directly prior to each data-set acquisition. Due to the higher number of AC voltages, the acquisition using the PZT probe was divided into two data-sets to make the time each syringe spent in the infusion pump comparable for each data-set. Thus, 3 data-sets were acquired; 6 V to 60 V with the CMUT, and 6 V to 26 V as well as 26 V to 90 V with the PZT array.

C. Calculation of CTR

The collected data from both probes were matched filtered and beamformed using delay-and-sum beamforming. CEUS images were composed using both (7) and (8). The two-pulse AM sequence, which was also studied by the authors in (Oygard et al., 2020b), is included for comparison with the three-pulse AM proposed by Fouan and Bouakaz (Fouan and Bouakaz, 2016), to study how an additional emission in the minor sequence affects the image quality. In addition, the data from every full amplitude emission in the minor sequence was used to compose B-mode images, for comparison. For each composed image, the CTR was calculated as

$$CTR = \frac{P_B}{P_{TMM}}, \qquad (12)$$

where P_B is the average power of the signal scattered by the bubbles and P_{TMM} is the average power scattered by the tissue-mimicking material. The average power was calculated as

$$P = \frac{1}{L_2 - L_1} \frac{1}{k_2 - k_1} \sum_{l=L_1}^{L_2} \sum_{m=k_1}^{k_2} y_{l,m}^2, \qquad (13)$$

where y is the signal in a single beamformed line of data, m is the sample number, k_1 and k_2 are sample numbers determining the axial position for the signal, and L_1 and L_2 are line numbers. Thus, the power was calculated in two rectangular regions-of-interest (ROIs). After beamforming the collected data, the ROIs used to calculate power in (13) were drawn around the channel in the phantom. The ROI in the tissue-mimicking phantom was taken to be the same size as the channel ROI, and placed at the same depth, in the middle of the tissue-mimicking phantom.

D. Hydrophone recordings

The derivation of (10) assumes that the same signal is produced by the full emission as the two half emissions combined. Array effects could arguably make the assumption fail if emission from one CMUT cell affects the emission from a neighbouring cell. It has been shown that the emission from an array of CMUTs is dependent on the distance between adjacent cells (Meynier et al., 2010). This distance varies between the emissions in the proposed sequences; in the full amplitude emissions the distance is one pitch, while in the half amplitude emissions it is $2 \cdot$ pitch. To evaluate if this effect adversely affects the similarity of the emitted pulses, and thus the cancellation of received linear terms, the signals emitted by each virtual source were recorded using a hydrophone. The hydrophone was placed in a water tank directly beneath the transducer, at $(y, z) = (0, 25)$ mm and moved to the x-positions corresponding to each virtual source, given by (11). The hydrophone recorded the minor sequence using all the applied AC voltages, from each virtual source. Then, the sequence's ability to cancel linear

terms was quantified by defining an annihilated power ratio as

$$\text{Annihilated power ratio} = \frac{\Sigma p_A^2 - \Sigma p_{AM}^2}{\Sigma p_A^2}. \quad (14)$$

Here, the numerator contains the remaining AM signal subtracted from the full emitted signal and thus gives the power of the annihilated signal. For each x-position and applied V_{AC}, the recordings of the minor sequence were used to compose the compounded emitted AM signal, p_{AM}, according to (7), and the annihilated power ratio. This evaluation will be affected by nonlinear propagation in the water. The evaluation was therefore performed using both the PZT array and CMUT for comparison, to distinguish effects caused by nonlinear propagation from the effects caused by nonlinear excitation.

In addition, the measured hydrophone signals were used to quantify the PNP caused by each applied V_{AC} for both transducers. The minimum of the recording of the full emission was found from the recording beneath each virtual source and averaged to give the PNP.

E. Quantifying signal-to-noise ratio

Because the imaging performance of a CMUT and a PZT transducer are to be compared, it is prevalent to also quantify and compare the signal-to-noise ratio (SNR) of the two transducers. The three-pulse AM imaging sequence was used to acquire $N = 10$ frames of a speckle phantom with $0.5\,\text{dB}\,\text{cm}^{-1}\,\text{MHz}^{-1}$ attenuation. Only the full emission was used to beamform B-mode images of the phantom, using the same axial sampling and depths as the images acquired of the microflow phantom in Section III B. The acquisition was repeated using both the PZT transducer and the CMUT for the range of applied AC voltages specified in Section III B, with a step-size of $10\,\text{V}$. After beamforming, the power of an image line located at $x = 0$ was extracted from the images, and the SNR was quantified as

$$\text{SNR} = \frac{1}{N}\sum_{N=1}^{10} \frac{\sum_{m=k_1}^{k_2} \overline{y}^2}{\sum_{m=k_1}^{k_2} (y - \overline{y})^2}, \quad (15)$$

where y is the image line and $\overline{y}$ represents the average of the image line across the 10 acquisitions.

IV. RESULTS

Fig. 3 shows examples of a B-mode image and both a two-pulse and a three-pulse AM image of the microflow phantom and tissue-mimicking material, where the chosen ROIs are drawn on top of the images. In the images, it is clear that both the AM sequences with both probes have succeeded in removing most of the speckle pattern from the tissue-mimicking phantom, whereas the signal from the microbubbles remain. More speckle pattern remains in the AM images composed with two pulses, indicating that the three-pulse sequence outperforms the

two-pulse sequence. The similarity of the images collected with the CMUT, in the left column of Fig. 3, and the PZT transducer, in the right column, gives a clear indication that CEUS with a CMUT is possible, despite the nonlinear nature of the probe.

Equations (12) and (13) were applied to all the collected images, both in three-pulse AM, two-pulse AM, and B-mode to calculate their CTR. The mean and standard deviation of the CTR was calculated for each set of 10 frames collected with constant V_{AC}. Fig. 4 shows the resulting mean CTR values with standard deviations as a function of V_{AC} applied to the CMUT for the three-pulse AM and B-mode, in addition to the difference between the two in decibels. Comparing the two modes shows that the CMUT has achieved a significant contrast enhancement across all the applied AC voltages, with 30 - 38 dB higher CTR in the CEUS images than in the B-mode.

Although the theory of the three-pulse AM sequence, presented in Section II, predicts that CTR should not degrade as the amount nonlinearity in the emitted signal rises with the applied AC voltage, it is expected that the CTR varies with AC voltage due to the nature of the microbubble contrast agents. As the applied voltage increases, so does the PNP of the emitted signal, which affects both the power and the spectral content of the scattered signal from the microbubbles (de Jong *et al.*, 2009). Therefore, to fully understand the observed variation in CTR seen in Fig. 4, in Fig. 5, the CTR values are also plotted as a function of the emitted PNP, as recorded by the hydrophone measurements. In addition, the CTR of the B-mode and CEUS images collected using the PZT probe are plotted, to provide a reference of how the CTR varies with PNP when the emission from the probe is linear. The CTR for the PZT array is divided into two data-sets, representing the images collected with separate syringes of SonoVue.

The compounded AM signals were computed from the collected hydrophone recordings, using (7), and the annihilated power ratio was calculated as in (14). Fig. 6 shows how the power ratio varies with PNP. Had the cancellation of the signals been completely successful, all power would be removed and the power ratio would be 100 %. That is not the case, and it can be seen that the power ratio declines as PNP increases above approximately $455\,\text{kPa}$. In the region where the two probes' PNP overlap, the power ratios of both the PZT transducer and the CMUT are high, indicating that the emitted signals are suitable for CEUS imaging, and that the efficiency of the three-pulse sequence is not affected by the increase in nonlinearity in the emitted signal from the CMUT, as the AC voltage is increased.

Finally, the SNR of the image acquisition using the two probes at varying AC voltages were calculated according to (15). The measured SNR is given in Table III. Generally, it is seen that the SNR of the CMUT probe is lower than the PZT transducer, with a mean difference of 16 dB across $6\,\text{V}$ to $56\,\text{V}$ applied AC voltage. Further discussion of the data will be given in Section V.
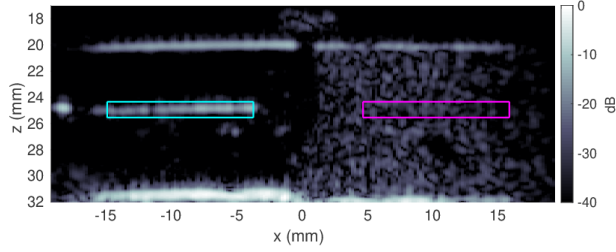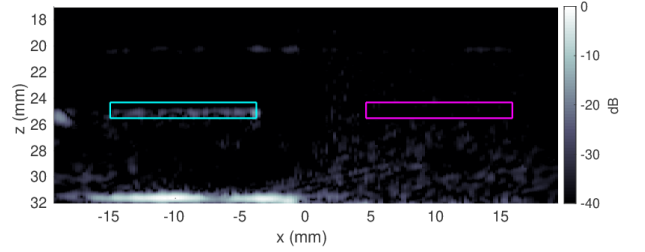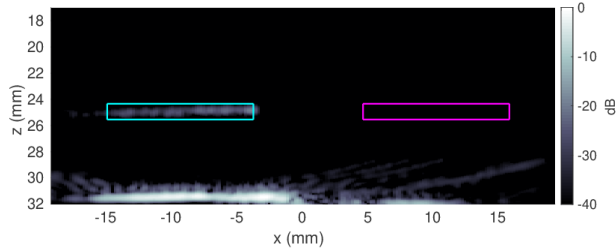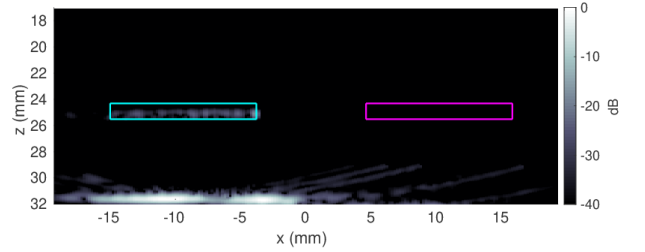
(a) CMUT: B-mode
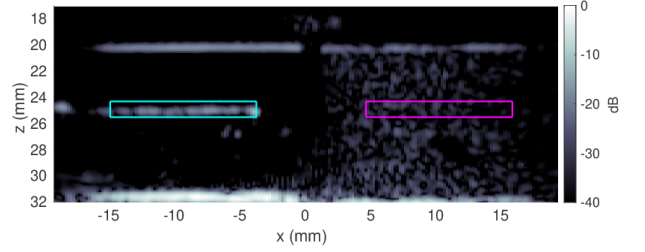
(b) PZT: B-mode
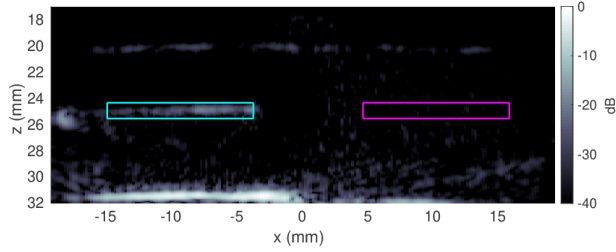
(c) CMUT: two-pulse amplitude modulation

(d) PZT: two-pulse amplitude modulation

(e) CMUT: three-pulse amplitude modulation

(f) PZT: three-pulse amplitude modulation

FIG. 3. Example images of the experimental set-up collected with the CMUT probe (left column) and PZT transducer (right column). Comparing the B-mode (a and b) with the two-pulse AM images (c and d) and the three-pulse AM image (e and f) show that the three-pulse sequence has successfully removed the speckle pattern inside the tissue-mimicking material (on the right of the image), while retaining the signal from the microbubbles (on the left of the image). The magenta and cyan boxes show the regions of interest used to calculate the CTR.

TABLE III. The measured SNR of the CMUT and PZT arrays across all of the applied AC voltages. The SNR is calculated according to (15) and displayed with $\pm$ one standard deviation, σ.

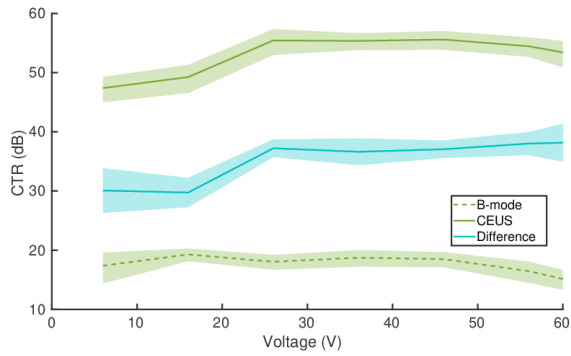| AC voltage (V)	6	16	26	36	46	56	60	66	76	86	90
CMUT SNR $\pm \sigma$ (dB)	37 ± 4	50 ± 6	61 ± 7	65 ± 6	71 ± 6	72 ± 6	72 ± 6	N/A	N/A	N/A	N/A
PZT SNR $\pm \sigma$ (dB)		71 ± 5	64 ± 4	75 ± 5	80 ± 6	81 ± 7	84 ± 5	N/A	87 ± 5	92 ± 5	92 ± 5	85 ± 5

FIG. 4. The calculated CTR values of the images collected with the CMUT using the three-pulse AM sequence, as a function of the applied AC voltage. The shaded areas indicated ± one standard deviation, calculated from the repeated acquisitions at each applied AC voltage. The green lines give the CTR of the CEUS and B-mode images, while the blue line gives the difference between the two.
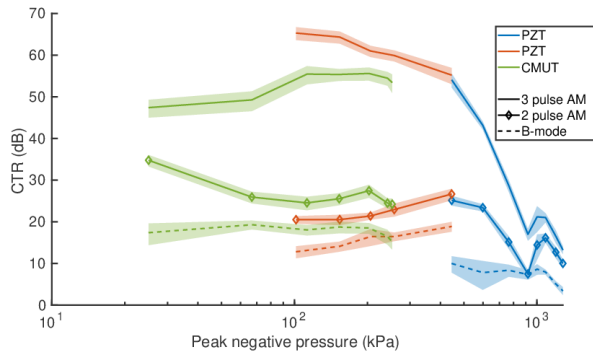

FIG. 5. The calculated CTR values of the images collected with the CMUT and PZT transducer, as a function of the emitted peak-negative-pressure. The CTR of three-pulse AM images are plotted with solid lines, of the two-pulse AM images with solid lines with diamonds, and the CTR of the B-mode images are plotted with dotted lines. The shaded areas indicated ± one standard deviation, calculated from the repeated acquisitions at each applied AC voltage.

V. DISCUSSION

As predicted by the theory laid out in Section II, Fig. 4 shows that the CTR of the CEUS images collected with the CMUT using the three-pulse AM sequence is not affected by the increase in nonlinear emission caused by an increasing AC voltage. There is a significant enhancement of contrast between the CEUS images and the B-mode images, with an average of 35.3 dB enhance-
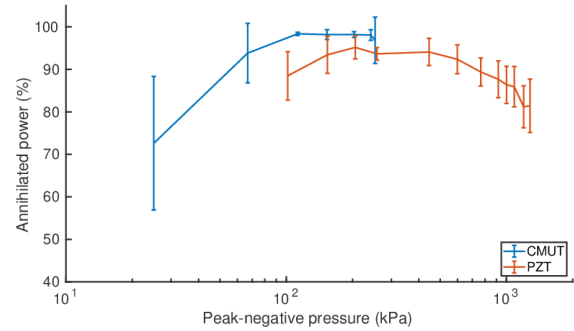

FIG. 6. The average percentage ratio of power annihilated in the AM signal, normalized to the emitted power. A power ratio of 100 % indicates that all of the power in the AM signal was removed. Error bars indicate ± one standard deviation of variation along VS positions.

ment across the applied voltages. Moreover, although the CTR of the CEUS images shown in Fig. 4 declines above 46 V, the difference between the logarithm of the CTR of the CEUS images and the B-mode images increases from 26 V to 60 V, demonstrating that the enhancement of the contrast caused by the three-pulse AM sequence is not affected by the applied AC voltage. On the other hand, it can bee seen in Fig. 5 that the two-pulse AM sequence has not accomplished the same enhancement. Clearly, reducing the number of emissions in the minor sequence, would benefit the frame rate. However, the average difference in CTR between the CEUS images and the B-mode images for the two-pulse AM sequence is only 9.1 dB. Thus, CEUS imaging using a CMUT should use the three-pulse AM sequence, despite the decrease in frame rate this will lead to.

The CTR of the CEUS images follows the expected trend; it increases initially, before starting to decrease at higher voltages. This progression is caused by the back-scattering properties of microbubbles. At low pressures, the nonlinear component of the back-scattering from microbubbles is proportional to the incident acoustic pressure (de Jong *et al.*, 2009; Marmottant *et al.*, 2005), and Emmer et al. (Emmer *et al.*, 2007) showed that SonoVue exhibits a low pressure threshold, under which the bubbles do not scatter nonlinearly. On the other hand, at high pressures, the CTR is expected to drop because the microbubbles start to degrade, through processes such as rupture of the lipid shell, diffusion of the gas core, or fragmentation (Chomas *et al.*, 2001; Dayton *et al.*, 1999; Thomas *et al.*, 2012). A decline in CTR of the CEUS images collected with the CMUT is observed in Fig. 4 starting at 46 V, and correspondingly in Fig. 5 at 203 kPa. However, this decline in CTR does not point to a failure of the three-pulse AM sequence, but rather a natural consequence of the properties of the microbubbels. According to de Jong et al. (de Jong *et al.*, 2009), SonoVue

can withstand up to 150 kPa before it starts to deform, and it is destroyed with a few repeated ultrasound exposures above approximately 300 kPa. This corresponds to the range at which the CTR in Fig. 5 starts to decline, taking into account the attenuation the emitted signal will experience before reaching the microbubbles inside the phantom. Thus, it has been shown that the ideal pressure range to perform CEUS imaging with a CMUT lies approximately between 100 kPa to 200 kPa.

Moreover, the same downwards trend in CTR of the CEUS images above approximately 100 kPa is observed for the images collected using the PZT transducer as for the images collected using the CMUT, further reinforcing that the decline is not caused by a deterioration of the three-pulse AM sequence. The PZT transducer displays a rapid decline in CTR above 455 kPa, likely caused by both the microbubble disruption discussed above, but also by nonlinear propagation in the image medium. The ratio of annihilated power shown in Fig. 6 also declines above 455 kPa, pointing to a discrepancy in the emitted pulses. Observation of the recorded hydrophone signals reveal saw-tooth like pulse shapes, indicative of nonlinear propagation (Hamilton and Blackstock, 1998). This distortion of the emitted pulses will differ between the full amplitude and half amplitude emissions, and thus cause the cancellation in (7) to fail.

Although the same AC voltage was applied to the CMUT and the PZT transducer, up to the maximum tolerable AC voltage of the CMUT, the PZT transducer emits higher PNP than the CMUT. The two probes have some overlap in their area of operation between 101 kPa to 258 kPa. In this region, both probes exhibit a significant contrast enhancement, with an average difference in CTR between the CEUS images and the B-mode images of 49.9 dB and 37.4 dB for the PZT transducer and CMUT, respectively. The fact that the PZT transducer overall performs better contrast enhancement than the CMUT is likely caused by the PZT transducer's superior SNR. At a constant emitted pressure, the back-scattering from the microbubbles will generally be the same for the PZT transducer and CMUT. Yet, the CTR can differ, if the amount of received noise is higher for the CMUT. As shown in Table III the CMUT has a lower SNR than the PZT transducer at all applied voltages. This is expected, since the probe is built in-house, whereas the PZT transducer is a commercial probe and has superior shielding from electromagnetic interference noise.

Yet, the quantification of the annihilated power shown in Fig. 6 shows that the CMUT generally outperforms the PZT transducer. The power annihilation ratio quantifies how much power that remains in the compounded emission and thus gives an indication of how well the transducers are able to perform contrast enhancement imaging. The cancellation of the emitted pulses is more effective for the CMUT than the PZT transducer, indicating that array effects in the CMUT is not causing significant degradation of the contrast enhancement. In the region where the two probes' PNPs overlap, the compounding of the AM signal from the CMUT leaves an average of 2 % of the emitted power, while for the PZT transducer the average remaining power is 7 %. When using the emissions for imaging, the amount of remaining power will transfer to the scattered signals and impair the ability to cancel linear signal from the tissue, thus lowering the CTR. Moreover, both probes exhibit an increase in the annihilated power with applied AC voltage, as well as an increased standard deviation of the annihilated power at low applied AC voltages. This further supports that the nonlinear emission from the CMUT does not negatively impact the creation of CEUS images using the proposed three-pulse AM sequence.

VI. CONCLUSION

Investigation of the creation of CEUS images with a CMUT has shown that the probe's inherent nonlinearity does not affect its performance, and that high contrast CEUS images can be created using a three-pulse AM sequence. The fact that the performance of the CMUT probe is not dependent on the harmonics of its emissions has been demonstrated theoretically, using quantification of CTR of CEUS images of microbubbles, and using hydrophone measurements of the emitted signals. Theoretically, it has been shown that there is no reason why the emitted harmonics will affect the CEUS images. This was confirmed by the acquired CEUS images, where an average of 37.4 dB contrast enhancement was achieved, using the three-pulse AM sequence. Comparison of the CTR of the images obtained using the proposed three-pulse AM sequence with the CTR of images obtained using only 2 emissions showed a significant advantage of the three-pulse AM, as the two-pulse AM sequence gave only an average of 9.07 dB contrast enhancement. Thus, a higher number of emissions in the minor sequence must be used, despite its negative impact on the frame rate. Further, comparison of the performance of the CMUT with a PZT transducer of similar design showed a comparable amount of contrast enhancement, as the images produced with the PZT transducer achieved an average of 49.9 dB contrast enhancement. The PZT transducer achieved higher CTR, but also higher SNR, and improvement of the design of the CMUT, especially focused on noise shielding, will likely improve its contrast enhancement abilities. Finally, hydrophone recordings and quantification of the annihilated power in the minor sequence showed that in the region of overlapping PNPs, the CMUT annihilated 98 % of the power, whereas the PZT transducer only annihilated 93 %. Thus, more power was cancelled in the CMUT's minor sequence than in the PZT transducer's, further reinforcing that the difference between the CTR produced by the CMUT and the PZT transducer is caused by the probes respective receive capabilities, rather than the emitted harmonics. Thus, future use of CMUT technology for CEUS images show great potential, and it will be possible to take advantage of the wide bandwidth, low emission pressure, and favorable sensitivity features of CMUTs for CEUS imaging.

VII. APPENDIX

The tree emissions given in (3) - (5) can be written on the compact form seen in (2) as

$$p_A(t) = p_L + \sum_{h=2}^{\infty} p_H, \qquad (16)$$

$$p_B(t) = 0.5\, p_L + 0.5 \sum_{h=2}^{\infty} p_H, \qquad (17)$$

$$p_C(t) = 0.5\, p_L + 0.5 \sum_{h=2}^{\infty} p_H. \qquad (18)$$

The emissions in this form are inserted into (9);

$$
\begin{aligned}
y_{AM}(t) = &\, a_1 p_A + a_2 p_A{}^2 + a_3 p_A{}^3 \\
&- a_1 p_B - a_2 p_B{}^2 - a_3 p_B{}^3 \\
&- a_1 p_C - a_2 p_C{}^2 - a_3 p_B{}^3
\end{aligned}
\qquad (19)
$$

$$
\begin{aligned}
= &\, a_1 \left(p_L + \sum_{h=2}^{\infty} p_H \right) + a_2 \left(p_L + \sum_{h=2}^{\infty} p_H \right)^2 \\
&+ a_3 \left(p_L + \sum_{h=2}^{\infty} p_H \right)^3 - a_1 \left(0.5 p_L + 0.5 \sum_{h=2}^{\infty} p_H \right) \\
&- a_2 \left(0.5 p_L + 0.5 \sum_{h=2}^{\infty} p_H \right)^2 - a_3 \left(p_L + \sum_{h=2}^{\infty} p_H \right)^3 \\
&- a_1 \left(0.5 p_L + 0.5 \sum_{h=2}^{\infty} p_H \right) \\
&- a_2 \left(0.5 p_L + 0.5 \sum_{h=2}^{\infty} p_H \right)^2 - a_3 \left(p_L + \sum_{h=2}^{\infty} p_H \right)^3.
\end{aligned}
\qquad (20)
$$

Canceling terms and expanding the parenthesis gives

$$
\begin{aligned}
y_{AM}(t) = &\, 0.5\, a_2\, p_L{}^2 + 0.5\, a_2 \left(\sum_{h=2}^{\infty} p_H \right)^2 \\
&+ a_2 p_L \left(\sum_{h=2}^{\infty} p_H \right) + 2.25\, a_3 p_L \left(\sum_{h=2}^{\infty} p_H \right)^2 \\
&+ 2.25\, a_3 p_L{}^2 \left(\sum_{h=2}^{\infty} p_H \right) \\
&+ 0.75\, a_3 \left(\sum_{h=2}^{\infty} p_H \right)^3 + 0.75\, a_3 p_L{}^3.
\end{aligned}
\qquad (21)
$$

The long form of (3) - (5) are then reintroduced;

$$
\begin{aligned}
y_{AM}(t) = &\, 0.5\, a_2 \sin(\omega_0 t)^2 \\
&+ 0.5\, a_2 \left(\sum_{h=2}^{\infty} \alpha_h \sin(h\omega_0 t + \phi_h) \right)^2 \\
&+ a_2 \sin(\omega_0 t) \left(\sum_{h=2}^{\infty} \alpha_h \sin(h\omega_0 t + \phi_h) \right) \\
&+ 2.25\, a_3 \sin(\omega_0 t) \left(\sum_{h=2}^{\infty} \alpha_h \sin(h\omega_0 t + \phi_h) \right)^2 \\
&+ 2.25\, a_3 \sin(\omega_0 t)^2 \left(\sum_{h=2}^{\infty} \alpha_h \sin(h\omega_0 t + \phi_h) \right) \\
&+ 0.75\, a_3 \left(\sum_{h=2}^{\infty} \alpha_h \sin(h\omega_0 t + \phi_h) \right)^3 \\
&+ 0.75\, a_3 \sin(\omega_0 t)^3.
\end{aligned}
\qquad (22)
$$

Finally, the last term of (22) is expanded to give

$$
\begin{aligned}
y_{AM}(t) = &\, 0.5\, a_2 \sin(\omega_0 t)^2 \\
&+ 0.5\, a_2 \left(\sum_{h=2}^{\infty} \alpha_h \sin(h\omega_0 t + \phi_h) \right)^2 \\
&+ a_2 \sin(\omega_0 t) \left(\sum_{h=2}^{\infty} \alpha_h \sin(h\omega_0 t + \phi_h) \right) \\
&+ 2.25\, a_3 \sin(\omega_0 t) \left(\sum_{h=2}^{\infty} \alpha_h \sin(h\omega_0 t + \phi_h) \right)^2 \\
&+ 2.25\, a_3 \sin(\omega_0 t)^2 \left(\sum_{h=2}^{\infty} \alpha_h \sin(h\omega_0 t + \phi_h) \right) \\
&+ 0.75\, a_3 \left(\sum_{h=2}^{\infty} \alpha_h \sin(h\omega_0 t + \phi_h) \right)^3 \\
&- 0.1875\, a_3 \sin(3\omega_0 t) + 1.5\, a_3 \sin(\omega_0 t).
\end{aligned}
\qquad (23)
$$

Bouakaz, A., Frigstad, S., Cate, F. T., and de Jong, N. (**2002**). "Super harmonic imaging: a new imaging technique for improved contrast detection," Ultrasound Med. Biol. **28**(1), 59–68.

Brock-Fischer, G. A., Poland, M. D., and Rafter, P. G. (**1996**). "Means for increasing sensitivity in non linear ultrasound systems" US Patent (5577505).

Certon, D., Teston, F., and Patat, F. (**2005**). "A finite difference model for CMUT devices," IEEE Trans. Ultrason., Ferroelec., Freq. Contr. **52**(12), 2199–2210.

Chomas, J. E., Dayton, P., Allen, J., Morgan, K., and Ferrara, K. (**2001**). "Mechanisms of contrast agent destruction," IEEE Trans. Ultrason., Ferroelec., Freq. Contr. **48**(1), 232–248.

Christensen-Jeffries, K., Browning, R. J., Tang, M., Dunsby, C., and Eckersley, R. J. (**2015**). "In vivo acoustic super-resolution and super-resolved velocity mapping using microbubbles," IEEE Trans. Med. Imag. **34**(2), 433–440.

Dayton, P., Morgan, K. E., Kilbanov, A. L., Brandenburger, G. H., and Ferrara, K. W. (**1999**). "Optical and acoustical observations

of the effects of ultrasound on contrast agents," IEEE Trans. Ultrason., Ferroelec., Freq. Contr. **46**(1), 220–232.

de Jong, N., Emmer, M., van Wame, A., and Versluis, M. (**2009**). "Ultrasonic characterization of ultrasound contrast agents," Med. Biol. Eng. Comp. **47**(8), 861–873.

Diederichsen, S. E. (**2020**). "Micromachined integrated transducers for ultrasound imaging," Ph.D. thesis, Denmark Technical University.

Dietrich, C. F., Averkiou, M., Nielsen, M. B., Barr, R. G., Burns, P. N., Calliada, F., Cantisani, V., Choi, B., Chammas, M. C., Clevert, D. *et al.* (**2018**). "How to perform contrast-enhanced ultrasound (CEUS)," Ultrasound international open **4**(1), E2.

Eckersley, R. J., Chin, C. T., and Burns, P. N. (**2005**). "Optimising phase and amplitude modulation schemes for imaging microbubble contrast agents at low acoustic power," Ultrasound Med. Biol. **31**(2), 213–219.

Emmer, M., van Wamel, A., Goertz, D. E., and de Jong, N. (**2007**). "The onset of microbubble vibration," Ultrasound Med. Biol. **33**, 941–949.

Errico, C., Pierre, J., Pezet, S., Desailly, Y., Lenkei, Z., Couture, O., and Tanter, M. (**2015**). "Ultrafast ultrasound localization microscopy for deep super-resolution vascular imaging," Nature **527**, 499–502.

Fouan, D., and Bouakaz, A. (**2016**). "Investigation of classical pulse sequences for contrast-enhanced ultrasound imaging with a CMUT probe," IEEE Trans. Ultrason., Ferroelec., Freq. Contr. **63**(10), 1496–1503.

Haller, M. I., and Khuri-Yakub, B. T. (**1994**). "A surface micromachined electrostatic ultrasonic air transducer," in *Proc. IEEE Ultrason. Symp.*, Vol. 2, pp. 1241–1244.

Hamilton, M. F., and Blackstock, D. T. (**1998**). *Nonlinear Acoustics* (Academic Press, San Diego).

Jensen, J. A., Nikolov, S., Gammelmark, K. L., and Pedersen, M. H. (**2006**). "Synthetic aperture ultrasound imaging," Ultrasonics **44**, e5–e15.

Kamaya, A., Machtaler, S., Sanjani, S. S., Nikoozadeh, A., Sommer, F. G., Khuri-Yakub, B. T., Willmann, J. K., and Desser, T. S. (**2013**). "New technologies in clinical ultrasound," Seminars in Roentgenology 214–223.

Kinsler, L. E., Frey, A. R., Coppens, A. B., and Sanders, J. V. (**1982**). *Fundamentals of Acoustics*, third ed. (John Wiley & Sons, New York).

Lai, S. S. M., Yiu, B. Y. S., Poon, A. K. K., and Yu, A. C. H. (**2013**). "Design of anthropomorphic flow phantoms based on rapid prototyping of compliant vessel geometries," Ultrasound Med. Biol. **39**(9), 1654–1664.

Lei, A., Diederichsen, S. E., Hansen, S. M., Stuart, M. B., Bagge, J. P., Jensen, J. A., and Thomsen, E. V. (**2016**). "Elimination of second-harmonics in CMUTs using square pulse excitation," in *Proc. IEEE Ultrason. Symp.*, pp. 1–4.

Leighton, T. (**1994**). *The Acoustic Bubble* (Elsevier Inc., London).

Lohfink, A., and Eccardt, P. C. (**2005**a). "Investigation of nonlinear CMUT behavior," in *Proc. IEEE Ultrason. Symp.*, pp. 585–588.

Lohfink, A., and Eccardt, P.-C. (**2005**b). "Linear and nonlinear equivalent circuit modeling of CMUTs," IEEE Trans. Ultrason., Ferroelec., Freq. Contr. **52**(12), 2163–2172.

Marmottant, P., van der Meer, S., Emmer, M., Verskuis, M., de Jong, N., Hilgenfe, S., and Lohse, D. (**2005**). "A model for large amplitude oscillations of coated bubbles accounting for buckling and rupture," J. Acoust. Soc. Am. **118**, 3499–3505.

Martin, K. H., Lindsey, B. D., Ma, J., Lee, M., Li, S., Foster, F. S., Jiang, X., and Dayton, P. A. (**2014**). "Dual-frequency piezoelectric transducers for contrast enhanced ultrasound imaging," Sensors 20825–20842.

Meynier, C., Teston, F., and Certon, D. (**2010**). "A multiscale model for array of capacitive micromachined ultrasonic transducers," J. Acoust. Soc. Am. **128**(5), 2549–2561.

Miller, D. L. (**1981**). "Ultrasonic detection of resonant cavitation bubbles in a flow tube by their second-harmonic emissions," Ultrasonics **19**, 217–224.

Novell, A., Bouakaz, A., Legros, M., and Felix, N. (**2008**). "Nonlinear contrast imaging with capacitive micromachined transducers," Proc. IEEE Ultrason. Symp. .

Novell, A., Bouakaz, A., Legros, M., and Felix, N. (**2009**). "Exploitation of capacitive micromachined transducers for nonlinear ultrasound imaging," Proc. IEEE Ultrason. Symp. 2733–2743.

Olesen, J. B., Villagómez Hoyos, C. A., Møller, N. D., Ewertsen, C., Hansen, K. L., Nielsen, M. B., Bech, B., Lönn, L., Traberg, M. S., and Jensen, J. A. (**2018**). "Non-invasive estimation of pressure changes using 2-D vector velocity ultrasound: An experimental study with in-vivo examples," IEEE Trans. Ultrason., Ferroelec., Freq. Contr. **65**(5), 709–719.

Ommen, M. L., Schou, M., Zhang, R., Hoyos, C. A. V., Jensen, J. A., Larsen, N. B., and Thomsen, E. V. (**2018**). "3D printed flow phantoms with fiducial markers for super-resolution ultrasound imaging," in *Proc. IEEE Ultrason. Symp.*, pp. 1–4.

Oralkan, O., Ergun, A. S., Johnson, J. A., Karaman, M., Demirci, U., Kaviani, K., Lee, T. H., and Khuri-Yakub, B. T. (**2002**). "Capacitive micromachined ultrasonic transducers: Next-generation arrays for acoustic imaging?," IEEE Trans. Ultrason., Ferroelec., Freq. Contr. **49**, 1596–1610.

Oygard, S. H., Ommen, M. L., Engholm, M., Schou, M., Diederichsen, S. E., Thomsen, E. V., Stuart, M. B., and Jensen, J. A. (**2020**a). "Investigating a CMUT's ability to achieve non-linear contrast enhancement," in *Proc. IEEE Ultrason. Symp.*, pp. 1–4.

Oygard, S. H., Ommen, M. L., Engholm, M., Schou, M., Diederichsen, S. E., Thomsen, E. V., Stuart, M. B., and Jensen, J. A. (**2020**b). "Investigating a CMUT's ability to achieve non-linear contrast enhancement," in *Proc. IEEE Ultrason. Symp.*, pp. 1–4.

Savoia, A. S., Caliano, G., and Pappalardo, M. (**2012**). "A CMUT probe for medical ultrasonography: From microfabrication to system integration," IEEE Trans. Ultrason., Ferroelec., Freq. Contr. **59**(6), 1127–1138.

Simpson, D. H., Chin, C. T., and Burns, P. N. (**1999**). "Pulse inversion Doppler: A new method for detecting nonlinear echoes from microbubble contrast agents," IEEE Trans. Ultrason., Ferroelec., Freq. Contr. **46**(2), 372–382.

Tang, M. X., Mulvana, H., Gauthier, T., Lim, A. K. P., Cosgrove, D. O., Eckersley, R. J., and Stride, E. (**2011**). "Quantitative contrast-enhanced ultrasound imaging: a review of sources of variability," Interface Focus **1**(4), 520–539.

Thomas, D. H., Butler, M., Anderson, T., Emmer, M., Vos, H., Borden, M., Stride, E., de Jong, N., and Sboros, V. (**2012**). "The quasi-stable lipid shelled microbubble in response to consecutive ultrasound pulses," Appl. Phys. Lett. **101**(7).

Zhou, S., Reynolds, P., and Hossack, J. (**2003**). "Pre-compensated excitation waveform to suppress second harmonic generation in MEMS electrostatic transducers," in *Proc. IEEE Ultrason. Symp.*, pp. 477–480.